Effects of PEM Thickness on Cold-Start Performance of PEMFC under Low-Temperature Conditions

Bintao Li, Qian Hong, Binbin Sun, Pengwei Wang, Hongyan Wang

Abstract—**During the cold-start operation of proton exchange membrane fuel cells (PEMFC) at a low temperature, the product water from electrochemical reactions tends to freeze, blocking porous electrodes and ultimately causing cold start failure. To effectively overcome this challenge, a comprehensive three-dimensional, transient, multi-physics coupled numerical simulation model was strategically developed using COMSOL Multiphysics to thoroughly analyze PEMFC cold-start behavior. The model enables systematic investigation of how proton exchange membrane (PEM) thickness affects current density distribution, ice formation dynamics, and thermal evolution characteristics during subzero cold-start processes. Experimental validation was conducted with three PEM thicknesses (0.05 mm, 0.127 mm and 0.183 mm) at -20 °C, Data analysis revealing that when the PEM thickness increased from 0.05 mm to 0.183 mm, the maximum current density of the PEMFC decreased from 0.126 A·cm⁻² to 0.061 A·cm⁻², while the cold-start duration extended from 37.9 s to 76 s. Significantly, the 0.127-mm PEM demonstrated the highest temperature rise among the three configurations, reaching 4.17 K. Although thicker PEM prolonged cold-start survival time and enhanced water retention, excessive thickness diminishes the cell's thermal mass and impairs temperature rise efficiency.**

Index Terms—**PEMFC; current density; cold-start; PEM thickness; maximum temperature rise**

I. Introduction

PEMFC exhibits high energy conversion efficiency through direct conversion of reactants' chemical energy into electrical energy, producing only water and heat as byproducts, thereby achieving zero harmful emissions. Furthermore, PEMFC possesses advantages including high energy density, low-temperature operation performance and quiet performance, making them ideal power sources for automotive applications. However, PEMFC must endure complex operating environments involving challenges such as air impurity contamination, frequent start-stop cycles, and high-low current switching, which significantly hinder their widespread adoption. Among these challenges, low-temperatures cold-start performance constitutes a critical challenge. When cold start at sub-zero temperatures, the water produced by electrochemical reactions may freeze and block the pores in the porous electrodes (particularly in the catalyst layer), ultimately causing the electrochemical reactions and cold start failure.

Xu Peng identified water storage capacity (WSC) as a critical performance metric and established a comprehensive multiphase numerical model for PEMFC during cold-start conditions, employing a layered aggregation methodology. Their systematic investigation demonstrated that three key structural parameters significantly improve the cell's water retention capability: (1) an increased polymer volume fraction within the cathode catalyst layer (CCL), (2) greater thickness of the PEM, and (3) enhanced pore volume in the porous transport layers [1]. In a parallel investigation, Feng Jun et al. demonstrated that optimizing the catalyst layer's (CL) structural characteristics—specifically through increased thickness and higher Nafion content—can significantly delay ice formation within the porous architecture and potentially prevent complete pore blockage under freezing conditions [2]. Yang et al. conducted a comprehensive study focusing on mass transport, phase transition, and electrochemical reactions within the CL during cold-start conditions. Furthermore, their analysis demonstrated that a thicker CL enhances thermal and water retention, thereby increasing the critical ice volume fraction before failure. Conversely, a higher ionomer-to-carbon (I/C) ratio reduces CL porosity, which diminishes the critical ice fraction and accelerates performance degradation [3]. Pu He's research team developed a one-dimensional, multiphase, non-isothermal transient model to systematically evaluate the impact of platinum (Pt) loading in the CCL on fuel cell cold-start performance. Their numerical simulations revealed that increased Pt loading not only delays the onset of ice formation but also significantly reduces the ice accumulation rate during cold-start operation [4]. J. Zhao et al. developed a sophisticated one-dimensional transient multiphysics

Manuscript received April 14, 2025; revised July 10, 2025.

This work was supported in part by the Postdoctoral Science Foundation of Shandong under Grant ZR2024ME179, the Innovation team project of "Qing-Chuang science and technology plan" of colleges and universities in Shandong Province 2021K1083, Major Innovation Projects in Shandong under Grant 2020CXGC010405 and 2020CXGC010406.

Bintao Li is a graduate student of School of Transportation and Vehicle Engineering, Shandong University of Technology, Zibo, 255000 PR China (e-mail: 13968154214@163.com).

Qian Hong is a Lecturer of School of Mechanical and Electrical Engineering, Shandong Vocational College of Industry, Zibo, 256414 PR China (e-mail: 377762483@qq.com).

Binbin Sun is a Professor of School of Transportation and Vehicle Engineering, Shandong University of Technology, Zibo, 255000 PR China (Corresponding author to provide phone: 86-13708941464; e-mail: Sunbin_sdut@126.com).

Pengwei Wang is a Professor of School of Transportation and Vehicle Engineering, Shandong University of Technology, Zibo, 255000 PR China (Corresponding author to provide phone: 86-13287825788; e-mail: wpwk16@163.com).

Hongyan Wang is a graduate student of School of Transportation and Vehicle Engineering, Shandong University of Technology, Zibo, 255000 PR China (e-mail: 19811730129@163.com).

coupling model that systematically examines how constant-voltage and constant-current operational strategies affect the cold-start behavior of PEMFC. This comprehensive model integrates coupled electrochemical reactions, heat transfer mechanisms, and mass transport processes to elucidate the fundamental characteristics of cold-start operation across diverse working conditions. The simulation results reveal that the selection of output mode plays a pivotal role in determining cold-start performance, with particularly pronounced effects in subzero temperature environments. More specifically, the study demonstrates significant differences between these two operational approaches in terms of their impacts on three critical aspects: (1) the spatial and temporal evolution of temperature distributions within the cell, (2) the effectiveness of water management strategies, and (3) the kinetics of electrochemical reactions during the startup phase [5]. Yao Lei et al. developed a three-dimensional transient multiphase numerical model to investigate water transport phenomena in PEMFC. Through systematic computational analysis, their study demonstrated that an increased ionomer volume fraction in the CCL leads to enhanced water storage capacity utilization. [6]. Further relevant investigations have been conducted regarding cold-start performance optimization. Notably, Wei et al. [7] systematically examined the critical role of cooling circulation systems in facilitating successful low-temperature startup processes. In a related investigation of cold-start optimization strategies, Liao et al. [8] conducted a systematic analysis of gas channel geometry effects on fuel cell startup performance. Their computational and experimental study revealed that channel structural parameters significantly influence ice formation dynamics and reactant distribution during low-temperature operation. Yang et al. [9] established that increasing CL thickness promotes ohmic heating during cold-start operation. Their numerical simulations demonstrated that this thermal effect elevates the overall cell temperature while simultaneously suppressing localized ice crystallization in the CL microstructure, thereby improving cold-start capability. Ko et al. [10] conducted a comparative performance analysis between metallic and graphite bipolar plates in low-temperature fuel cell operation. Their experimental results demonstrated that metallic plates exhibit significantly faster temperature rise rates due to their enhanced thermal conductivity.

II. PEMFC COLD-START MODELLING

A. Numerical Modeling of Proton Exchange Membrane Cold Start

In this study, we develop a three-dimensional, multiphase flow-coupled multiphysics model to analyze the cold-start process of a PEMFC. To optimize computational efficiency, the geometric model represents a single serpentine-channel PEMFC with dimensions of 3.47 mm (length) × 2 mm (width) × 20 mm (height). Figure 1 illustrates the model structure, which comprises the following layers from top to bottom:

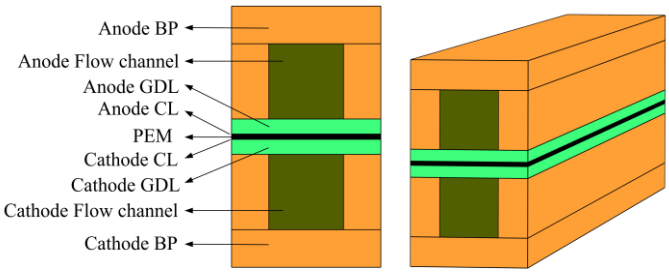

Fig. 1. Geometric model of PEMFC

The operation of a PEMFC involves multiple coupled physical and chemical mechanisms, including mass transport, fluid dynamics, heat transfer, electrochemical reactions, and phase transitions. To accurately simulate these processes, an appropriate selection of physical parameters is essential. The parameters for different physical fields (e.g., electrical conductivity, thermal conductivity, specific heat capacity, permeability, and porosity) are summarized in Table I.

TABLE I
GEOMETRIC AND PHYSICAL PARAMETERS OF PEMFC MODEL

Parameter	Value
PEM thickness (Nafion 112, Nafion 115, Nafion 117)	0.05; 0.127; 0.183 mm
equivalent mass of membrane	1100g·mol^{-1}
PEMFC membrane density	1980 kg·m^{-3}
CL thickness	0.01 mm
GDL thickness	0.2 mm
gas flow channel length; width; height	20; 1; 1 mm
CL, GDL porosity	0.3; 06
CL, GDL contact angle	100°; 120°
CL volume fraction of the ionomer	0.25
CL, GDL, BP conductivity	300; 300; 20000 S·m^{-1}
PEM, CL, GDL, BP heat conductivity	0.95; 1; 1; 20 W·m^{-1}·K^{-1}
PEM, CL, GDL, BP specific heat capacity	833;3300;568;1580J·kg^{-1}·K^{-1}
CL, GDL intrinsic penetration rate	6.2 x 10^{-13}; 6.2 x 10^{-12} m^2
outlet back pressure	1 atm
starting voltage	0.7 V
density of liquid water, ice	990; 920 kg·m^{-3}
specific heat capacity of hydrogen, oxygen, water vapor, liquid water, ice	14283; 919; 2014; 4182; 2060 J·kg^{-1}·K^{-1}
rate of evaporation, condensation, melting, sublimation	1 s^{-1}

mm = millimeter, mol = mole, kg = kilogram, V = volt, S = Siemens, m = meter, W = watt, K = kelvin, J = joule, atm = standard atmosphere, s = second.

B. Model Assumption

The low-temperature cold-start process of PEMFC contains several fields of research, and the following assumptions are made for this mathematical model to simplify the computational analysis of the model:

1) All gases involved in the reaction are considered ideal gases.
2) None of the reaction gases can be transported through the PEM.
3) The effect of gravity on the reacting gases inside the cell is not considered.
4) Ignore the sublimation of ice.
5) Ice in the pores of porous electrodes cannot move.
6) Frozen film state water cannot transport protons.
7) Charge/discharge characteristics of double layer capacitors without considering catalytic layer structure.

8) Structures such as PEM and electrodes are isotropic and homogeneous.
9) The fluid inside the fuel cell is a low-flow laminar and incompressible fluid.

C. Cold-Start Equations for Proton Exchange Membrane Fuel Cell

The control equations for PEMFC during cold start encompass the following aspects: mass conservation equation, momentum conservation equation, energy conservation equation, species conservation equation, and ionic charge conservation equation.

During operation of a PEMFC, electrochemical reactions involve coupled electron and ion transport. Ion transport occurs within the PEM and both cathode/anode catalyst layers, while electron transport takes place through the external circuit comprising the CL, gas diffusion layers (GDL), bipolar plates, and external load. Throughout this process, conservation of proton and electron potentials is maintained, as described by the following equation:

$$0 = \nabla \cdot (\kappa_e^{eff} \nabla \varphi_e) + S_e \quad (1)$$

$$0 = \nabla \cdot (\kappa_{ion}^{eff} \nabla \varphi_{ion}) + S_{ion} \; 0 = \nabla \cdot (\kappa_{ion}^{eff} \nabla \varphi_{ion}) + S_{ion} \quad (2)$$

Here, κ_{ion}^{eff}, $\kappa_{\mathrm{e}}^{\mathrm{eff}}$ are the effective ionic conductivity and effective electronic conductivity, respectively ($\mathrm{s \cdot m^{-1}}$), φ_{ion} is the ionic potential in the electrolyte, φ_{e} is the electron potential at the porous electrode and the polar plate ($\mathrm{s \cdot m^{-1}}$), S_{ion}, S_{e} are the ion source term and the electron source term, respectively ($\mathrm{A \cdot m^{-3}}$).

The conservation equation for the gas mixture is primarily solved in the CL, GDL and gas flow channel regions. The mass conservation equation for the gas mixture is given by Equation (3)::

$$\frac{\partial}{\partial t}\left(\varepsilon\left(1 - s_{\mathrm{lq}} - s_{\mathrm{ice}}\right)\rho_{\mathrm{g}}\right) + \nabla \cdot \left(\rho_{\mathrm{g}} \vec{u}_{\mathrm{g}}\right) = S_{\mathrm{m}} \quad (3)$$

Here, ε is the porosity of CL and GDL, ρ_{g} is the gas mixture density ($\mathrm{kg \cdot m^{-3}}$), s_{lq}, s_{ice} are the liquid water volume fraction and ice volume fraction, respectively, $\vec{u}_{\mathrm{g}}$ is the gas flow rate ($\mathrm{m \cdot s^{-1}}$), and S_{m} is the gas mixture mass source term ($\mathrm{kg \cdot m^{-3} \cdot s^{-1}}$), which is equal to the sum of the hydrogen and oxygen mass source terms and the water vapor mass source term.

To enhance the ionic conductivity of the electrolyte in fuel cells, the PEM and CL contain membrane-phase water, whose transport mechanism differs from that of gaseous and liquid water. The mass conservation equation for membrane-phase water is given by Equation (4):

$$\frac{\rho_{\mathrm{mem}}}{\mathrm{EW}} \frac{\partial}{\partial t}\left(\omega \lambda_{\mathrm{nf}}\right) = \frac{\rho_{\mathrm{mem}}}{\mathrm{EW}} \nabla \cdot \left(D_{\mathrm{mw}}^{\mathrm{eff}} \nabla \lambda_{\mathrm{nf}}\right) + S_{\mathrm{nfm}} \quad (4)$$

The left side of the equation represents the transient term, while the right side includes the diffusion term and the mass source term. ρ_{mem} denotes the dry state density of PEM ($\mathrm{g \cdot m^{-3}}$), EW denotes the equivalent mass of PEM ($\mathrm{g \cdot mol^{-1}}$), λ_{nf} denotes the water content of the membrane in the non-frozen membrane state, ω denotes the volume fraction of the CL ionomer, $D_{\mathrm{mw}}^{\mathrm{eff}}$ denotes the effective diffusion coefficient of the water in the non-frozen membrane state ($\mathrm{m^2 \cdot s^{-1}}$), and S_{nfm} is the source of the mass term of the water in the non-frozen membrane state ($\mathrm{kg \cdot m^{-3} \cdot s^{-1}}$).

During cold start, water within the electrolyte may also exist as ice, meaning the water in the electrolyte under subzero conditions is classified into unfrozen membrane-phase water and frozen membrane-phase water (i.e., membrane-ice). The conservation equation for membrane-ice is primarily solved in the electrolyte domains of the PEM and both CL, as expressed in Equation (5).

$$\frac{\rho_{\mathrm{mem}}}{\mathrm{EW}} \frac{\partial\left(\omega \lambda_{\mathrm{f}}\right)}{\partial t} = S_{\mathrm{fmw}} \quad (5)$$

Here, λ_f represents the content of frozen membrane water, and S_{fmw} represents the mass source term of the frozen membrane water.

Within PEMFC, liquid droplets form when water vapor concentration reaches saturation. While liquid water may theoretically appear wherever water vapor exists, this study assumes that liquid water only resides in the porous structures of the CL and GDL. Due to the high flow velocity in gas channels, it is postulated that any droplets would be rapidly removed by the gas stream; consequently, liquid water effects in flow channels are neglected. By further disregarding the negligible convective velocity of liquid water in the porous regions of CL and GDL, the conservation equation for liquid water in these domains, with water saturation (s) as the solution variable, is expressed in Equation (6).

$$\frac{\partial}{\partial t}\left(\rho_{\mathrm{lq}} \varepsilon s_{\mathrm{lq}}\right) = \nabla \cdot \left(\rho_{\mathrm{lq}} D_{\mathrm{lq}} \nabla s_{\mathrm{lq}}\right) + S_{\mathrm{lq}} \quad (6)$$

ρ_{lq} is the density of liquid water ($\mathrm{kg \cdot m^{-3}}$), D_{lq} is the diffusion coefficient of liquid water ($\mathrm{m^2 \cdot s^{-1}}$), S_{lq} and is the liquid water mass source term ($\mathrm{kg \cdot m^{-3} \cdot s^{-1}}$), which consists of two parts: the phase transition from water vapor to liquid water and the phase transition from liquid water to ice.

During the cold-start process of PEMFC, water is generated through electrochemical reactions at the cathode side and subsequently transported through the porous electrode and gas diffusion layer. Under subfreezing conditions, this water tends to freeze within the porous structures. The governing equation for ice formation is primarily solved in the computational domains of both the CL and gas diffusion layer, as represented by Equation (7).

$$\frac{\partial}{\partial t}\left(\rho_{\mathrm{ice}} \varepsilon s_{\mathrm{ice}}\right) = S_{\mathrm{ice}} \quad (7)$$

Here, ρ_{ice} is the ice bulk density ($\text{kg}\cdot\text{m}^{-3}$), s_{ice} is the ice volume fraction, S_{ice} is the ice mass source term, It consists of two components, the condensation icing source term from water vapor to ice and the solidification icing source term from liquid water to ice.

The momentum conservation equation is solved for the gaseous flow within the PEMFC, with its computational domain encompassing all gas transport regions except the PEM and bipolar plates. Specifically, this includes the gas flow channels, GDL, and CL. The governing momentum conservation equation for the gas phase is presented as Equation (8).

$$\begin{aligned}&\frac{\partial}{\partial t}\left(\frac{\rho_{\text{g}}\vec{u}_{\text{g}}}{\varepsilon\left(1-s_{\text{lq}}-s_{\text{ice}}\right)}\right)+\nabla\cdot\left(\frac{\rho_{\text{g}}\vec{u}_{\text{g}}\vec{u}_{\text{g}}}{\varepsilon^{2}\left(1-s_{\text{lq}}-s_{\text{ice}}\right)^{2}}\right)=-\nabla p_{\text{g}}\\&+\mu_{\text{g}}\nabla\cdot\left(\nabla\left(\frac{\vec{u}_{\text{g}}}{\varepsilon\left(1-s_{\text{lq}}-s_{\text{ice}}\right)}\right)+\nabla\left(\frac{\vec{u}_{\text{g}}^{T}}{\varepsilon\left(1-s_{\text{lq}}-s_{\text{ice}}\right)}\right)\right)\\&-\frac{2}{3}\mu_{\text{g}}\nabla\cdot\left(\nabla\left(\frac{\vec{u}_{\text{g}}}{\varepsilon\left(1-s_{\text{lq}}-s_{\text{ice}}\right)}\right)\right)+S_{\text{u}}\end{aligned}\tag{8}$$

Here, p_{g} is the gas-phase pressure (Pa), μ_{g} is the gas-phase kinetic viscosity ($\text{kg}\cdot\text{m}^{-1}\cdot\text{s}^{-1}$), and S_{u} is the momentum source term ($\text{kg}\cdot\text{m}^{-3}\cdot\text{s}^{-1}$).

The transport processes of gas species also occur within the flow field regions of the fuel cell. In the present model, the primary species considered are hydrogen, oxygen, and water vapor, with their transport phenomena being solved in the computational domains of gas flow channels, GDL and CL. The corresponding species conservation equations are given by Equation (9).

$$\begin{aligned}&\frac{\partial}{\partial t}\left(\varepsilon\left(1-s_{\text{lq}}-s_{\text{ice}}\right)\rho_{\text{g}}Y_{i}\right)+\nabla\cdot\left(\rho_{\text{g}}\vec{u}_{\text{g}}Y_{i}\right)\\&=\nabla\cdot\left(\rho_{\text{g}}D_{i}^{\text{eff}}\nabla Y_{i}\right)+S_{i}\end{aligned}\tag{9}$$

Here, *Yi* is the mass fraction of gas *i*, which consists of hydrogen, oxygen, water vapor and nitrogen, D_{i}^{eff} is the effective diffusion coefficient of gas component *i*, and S_{i} is the mass source term of each gas component, which indicates the mass consumption of the gas component in the electrochemical reaction process.

During the operation of PEMFC, heat generation occurs as an inherent byproduct. The internal thermal variations induce significant temperature fluctuations, which substantially impact the cell's operational performance. Consequently, energy-level modeling analysis of the fuel cell system becomes essential. The governing energy conservation equation is expressed in Equation (10).

$$\begin{aligned}&\frac{\partial}{\partial t}\left(\left(\rho C_{\text{p}}\right)_{\text{fl,sl}}^{\text{eff}}T\right)+\nabla\left(\left(\rho C_{\text{p}}\right)_{\text{fl}}^{\text{eff}}\vec{u}_{\text{g}}T\right)\\&=\nabla\cdot\left(k_{\text{fl,sl}}^{\text{eff}}\nabla T\right)+S_{\text{T}}\end{aligned}\tag{10}$$

Here, the first term to the left of the equal sign is the transient term and the second term is the convective heat transfer term. $\left(\rho C_{\text{p}}\right)_{\text{fl,sl}}^{\text{eff}}$ is the effective volumetric heat capacity ($\text{J}\cdot\text{kg}^{-1}\cdot\text{K}^{-1}$), $k_{\text{fl,sl}}^{\text{eff}}$ is the effective thermal conductivity ($\text{W}\cdot\text{m}^{-1}\cdot\text{K}^{-1}$), T is the temperature (K), and S_{T} is the energy source term, which mainly consists of the activation heat source term, the ohmic heat source term, the phase transition latent heat source term, and the electrochemical reversible heat source term.

D. Boundary Condition

During operation of PEMFC, the consumption rate of reactants is directly proportional to the current output. The inlet flow rates of reactant gases are determined based on the reference current density and the stoichiometric ratios of the cell. The mass flow rates of reactants at the anode and cathode inlets are specified by Equation (11).

$$\dot{m}_{\text{a}}=\frac{S_{\text{a}}\rho_{\text{g}}^{\text{a}}I_{\text{ref}}A_{\text{mem}}}{2Fc_{\text{H}_2}},\quad \dot{m}_{\text{c}}=\frac{S_{\text{c}}\rho_{\text{g}}^{\text{c}}I_{\text{ref}}A_{\text{mem}}}{4Fc_{\text{O}_2}}\tag{11}$$

Here, S represents the stoichiometric ratio of the supplied gas, ρ_{g} denotes the average density of the supplied gas, A is the reactive area of the fuel cell membrane electrode assembly, I_{ref} refers to the reference current density used for calculating gas flow rates, and F stands for Faraday's constant. Additionally, c_{H_2} and c_{O_2} correspond to the hydrogen concentration at the anode inlet and the oxygen concentration at the cathode inlet, respectively.

Convective heat transfer boundary conditions are applied at both ends and sides of the fuel cell electrodes (anode and cathode). The heat transfer rate between the external surfaces and the ambient environment is calculated using Equation (12).

$$\dot{Q}=hA_{\text{wall}}\left(T_{\text{surr}}-T_{\text{wall}}\right)\tag{12}$$

Here, h is the convective heat transfer coefficient of the surface,50 $\text{W}\cdot\text{m}^{-2}\cdot\text{K}^{-1}$, A_{wall} and T_{wall} denote the surface area and temperature of the facade, respectively, and T_{surr} denotes the ambient temperature.

The electric potential at the outer terminal of the anode-side bipolar plate is defined as the reference zero potential, while at the cathode-side bipolar plate terminal represents the output voltage. The thermodynamically reversible potential is described by the modified Nernst equation (13).

$$\begin{aligned}E_{r}&=1.23-0.9\times10^{-3}\left(T-T_{0}\right)\\&+\frac{RT}{2F}\ln\left(\frac{P_{\text{H}_2}P_{\text{O}_2}^{0.5}}{P_{\text{H}_2\text{O}}}\right)\end{aligned}\tag{13}$$

Here, T and T_0 refer to the actual temperature and the reference temperature at the site where the electrochemical reaction occurs respectively(298.15 K), K, ; R is the

universal gas constant; F is Faraday's constant; and P_{H_2} , P_{O_2} , and P_{H_2O} are the partial pressures of hydrogen, oxygen, and water vapor, respectively, in the fuel cell.

E. Numerical Method

In this study, we developed and solved the numerical model using *COMSOL Multiphysics®* finite element analysis software. Through the physics interface equation editor, we customized and modified the governing equations and key parameters. For the numerical solution, a segregated solution strategy was adopted and employed the PARDISO direct solver to handle the coupled Multiphysics field problem. To ensure numerical stability during computation, we employed the backward-differentiation formula for temporal discretization of the PEMFC's partial differential equations. The transient solution utilized an adaptive time-stepping strategy with a maximum step size constraint of 0.1 s. For nonlinear system resolution, we implemented the Newton-Raphson method with Jacobian matrix updates at each iteration to maintain solution accuracy and minimize error propagation. The transient solver's relative error tolerance was set to 0.005 — a more stringent criterion than the software's default value of 0.01 to enhance computational precision. All other solver parameters remained at their default software configurations.

F. Model Validation

To validate the reliability of the PEMFC cold-start model, comparative analyses were conducted under two characteristic operating conditions: room temperature (25 °C) and low temperature (-5 °C). As shown in Figure 2, the polarization curves obtained from experimental measurements show good agreement with model simulations in the low-to-medium current density range. However, discrepancies emerge at higher current densities, with a maximum observed deviation of 5%. These variations originate from necessary simplifications and idealizations in the modeling process. Importantly, the simulation results maintained consistent trends with experimental data, confirming the developed cold-start model can effectively predict PEMFC performance characteristics during low-temperature startup.

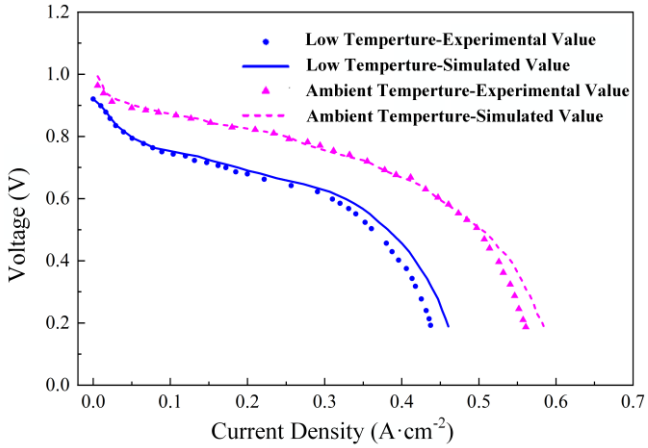

Fig. 2. Comparison of polarization curves between simulation and experiment

III. Effect of Proton Exchange Membrane Thickness on Cold-Start Performance of Fuel Proton Exchange Membranes

A. Current Density During Cold Start at Different Proton Exchange Membrane Thicknesses

Figure 3 demonstrated that the three PEM thickness configurations exhibited similar current density trends, showing an initial increase followed by a continuous decline. The results revealed an inverse relationship between PEM thickness and output current density. Specifically, the maximum current density decreases by approximately 50% from 0.126 A·cm^{-2} (0.050-mm PEM) to 0.061 A·cm^{-2} (0.183-mm PEM). Furthermore, PEM thickness significantly impacts cold-start duration, increasing from 37.9 s to 76 s as thickness grows from 0.050 mm to 0.183 mm.

The PEM thickness strongly correlates with the ohmic impedance of electrochemical reactions. Increasing PEM thickness elongates the proton transfer path and significantly raises proton transport resistance, thereby resulting in degraded current output performance under identical operating conditions. Conversely, reverse diffusion of bound water from the cathode to the anode driven by the water content gradient — is enhanced in thinner PEM due to their steeper gradients. This promotes bound water migration, mitigates anode-side membrane drying, and improves electrical output performance. Nevertheless, despite exhibiting lower current densities, thicker PEM exhibit lower current densities, reducing both water production and ice accumulation rates. While this prolongs the fuel cell's operational duration during cold-start operation, it may not guarantee a successful startup.

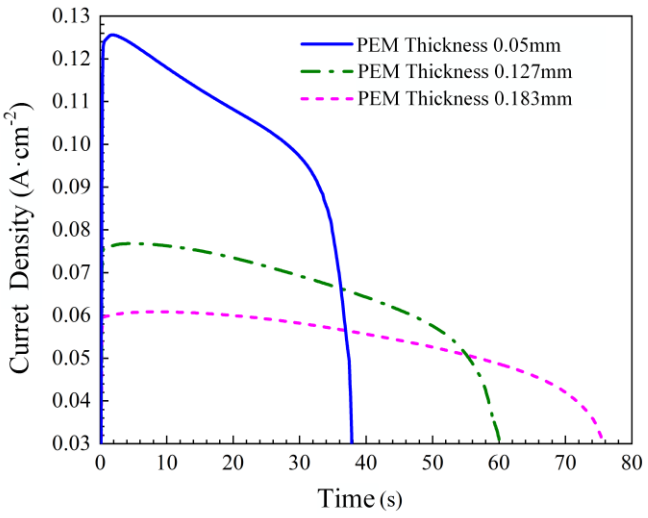

Fig. 3. Current density of cold start PEMFC with different PEM thicknesses

B. Ice Volume Fraction During Cold Start of PEMFC At Different Proton Exchange Membrane Thicknesses

Figure 4 illustrated the ice formation process in the CCL during cold-start operation with different PEM thicknesses. Due to the rapid accumulation of water and ice in the CCL of a straight-channel PEMFC during cold-start at -20 °C, all three cold-start cases failed within a short period. Simultaneously, the ice volume fraction near the flow channel inlet was relatively lower than in other regions, likely because the incoming air caused localized membrane drying in this area, thereby increasing water absorption and storage

in the membrane's ionomer and delaying ice formation after membrane water saturation. Comparing the ice volume fraction contours at different time steps, no ice formation was observed in the CCL of the PEMFC with a 0.183-mm PEM after 8 s, whereas localized ice volume fractions in the CCL of the PEMFC with a 0.05-mm PEM reached approximately 0.3. Increased PEM thickness delayed ice formation and extended the operational duration during cold-start conditions.

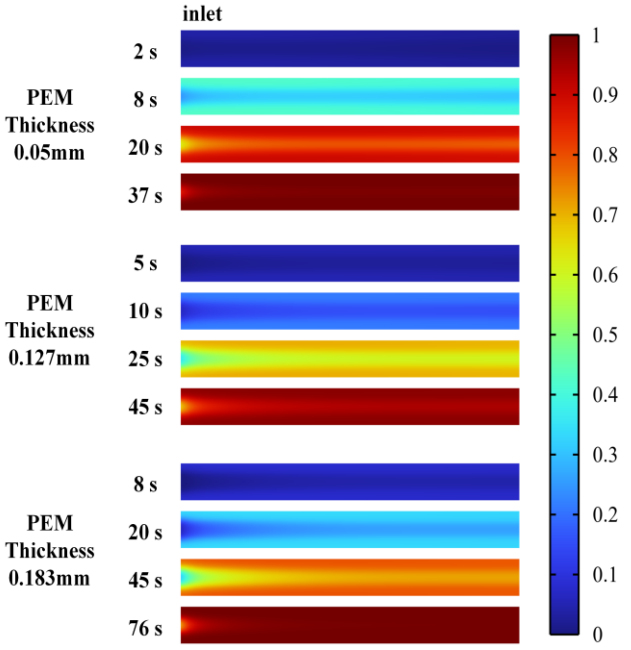

Fig. 4. Evolution of distribution of ice volume fraction in cathode CL during the cold-start processes of different PEM thicknesses

A comparison of the three PEM thickness configurations in Figure 5 revealed that varying the PEM thickness cannot prevent ice accumulation within the fuel cell during cold-start operation, as all cases ultimately failed at -20 °C. However, PEM thickness modification significantly alters the ionomer's water absorption capacity. The ice volume fraction curves in Figure 5 demonstrated that increased PEM thickness reduces the slope, indicating slower ice accumulation. This delay stems from the thicker PEM's higher absolute water storage capacity, which postpones the time required for ice to fully occupy the CL pore space. When the PEM thickness increased from 0.05 mm to 0.127 mm, the cold-start duration extended from 37.9 s to 60 s.

The ice formation dynamics in the CCL of PEMFC exhibit distinct spatial-temporal characteristics during cold-start operation. Initial ice nucleation predominantly initiates in the sub-rib regions proximal to the flow channel outlet during the early cold-start phase. Subsequent electrochemical reaction progression facilitates anisotropic ice propagation along the gas flow direction toward the inlet region, ultimately leading to pore occlusion within the porous electrode microstructure. Upon exceeding the critical ice volume fraction threshold, the PEMFC exhibits a rapid deterioration in current output concurrent with a measurable temperature reduction, ultimately resulting in cold start failure.

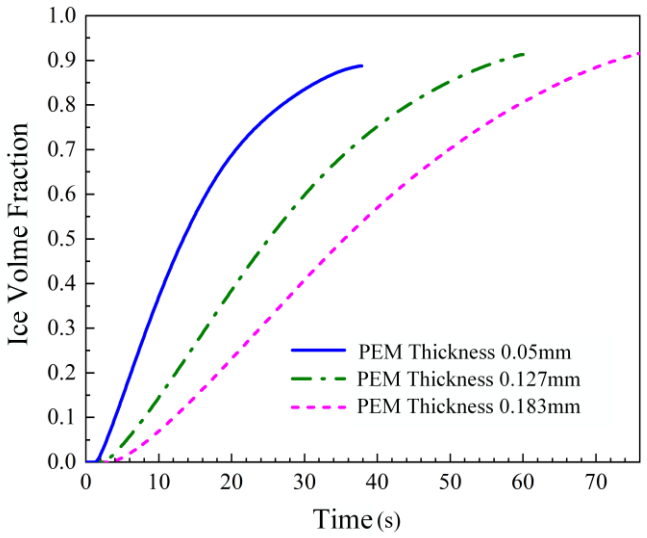

Fig. 5. Ice volume fraction of catalytic layers PEMFC with different film thicknesses

C. Temperature Changes During Cold Start of PEMFC At Different Proton Exchange Membrane Thicknesses

Figure 6 displays the temperature distribution contours at different time instants on the longitudinal cross-section along the central axis of the flow channel. The local maximum temperature consistently appears at the membrane electrode assembly, with a peak temperature increase of 4.17 K above the initial temperature occurring at 53 seconds during the cold-start process.

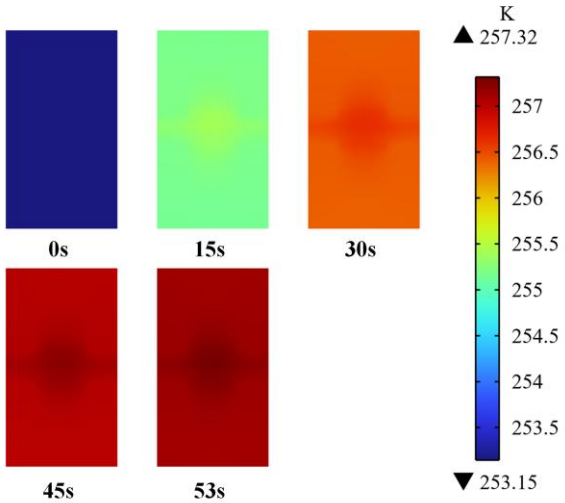

Fig. 6. Cell temperature at different moments (longitudinal section of the cell at the centered position in the lengthwise direction with a film thickness of 0.127 mm)

A comparison of the three temperature curves in Figure 7 reveals that the case with 0.05-mm PEM thickness exhibits the steepest slope in temperature rise, indicating the fastest initial heating rate. Increasing the PEM thickness results in a corresponding decrease in the slope of temperature curves, which demonstrates a reduced heating rate. Among these three configurations, the 0.183-mm PEM case shows the longest cold-start duration, while the 0.127-mm PEM exhibits the highest maximum temperature rise. This behavior can be attributed to two primary factors: First, as evidenced by the current density curves of the three PEM thickness configurations in Figure 3, fuel cells with thicker PEM generate lower output currents, resulting in reduced

electrochemical heat production. Second, increased PEM thickness elevates the overall heat capacity of the fuel cell system, leading to an adverse effect on the temperature rise rate. These findings suggest that while increasing PEM thickness can prolong cold-start duration, it does not fundamentally resolve cold-start challenges. Moreover, excessive thickness exacerbates thermal inertia, further increasing the system's heat capacity and reducing the temperature rise rate. Comprehensive analysis of the results indicates that the 0.127-mm PEM thickness offers more favorable cold-start performance compared to the 0.183-mm configuration.

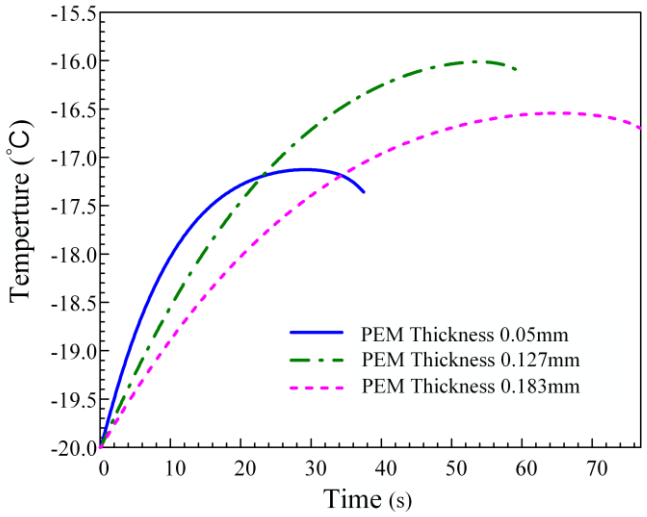

Fig. 7. Variation of the average temperature of PEMFC with different proton exchange film thicknesses

IV. Conclusion

This study investigates PEMFC. Based on the fundamental principles of fuel cell electrochemical reactions and heat/mass transfer theory and considering multiple water phase transition pathways within the cell. A transient multiphase model was developed to analyze fuel cell startup under subzero temperatures. The model was used to simulate transient cold-start processes at -20 °C, evaluating the effect of PEM thickness on cold-start performance. The main results can be summarized as follows:

Impact of PEM thickness: It was observed that increased PEM thickness significantly reduced the current output density of PEMFC while prolonging cold-start duration. However, excessively thick PEMs are not recommended for cold-start applications. From the perspective of temperature rise efficiency, the Nafion 115 membrane (0.127-mm thickness) demonstrates better suitability for PEMFC cold start compared to the Nafion 117 membrane (0.183-mm thickness). Key findings indicate that modifying PEM thickness cannot prevent ice accumulation within the fuel cell during cold-start operations, as all configurations ultimately failed at -20 °C. In contrast, PEM thickness variation alters the water absorption and storage capacity of the ionomer. Thicker PEM exhibit reduced ice accumulation rates, evidenced by flatter curved slopes. Their higher water storage capacity delays both ice nucleation and complete pore filling in the CL. Two competing mechanisms were identified:

1) Thicker PEM results in lower output currents, leading to reduced electrochemical heat generation.
2) Increased PEM thickness elevates the overall heat capacity of the fuel cell system, adversely affecting the temperature rise rate.

These results indicate that while increased PEM thickness can extend cold-start duration, it fails to overcome the key limitations in cold-start performance. Moreover, excessive PEM thickness may degrade thermal performance by increasing system heat capacity and slowing the temperature rise rate.

TABLE II
PEMFC COLD-START RESULTS OF THREE SCHEMES

PEM thickness	cold-start duration	maximum temperature rise
0.050mm	37.9s	2.85K
0.127mm	60.0s	4.17K
0.183mm	76.0s	3.40K

s = second, K = kelvin.

References

[1] P. Xu, S. Xu, X. Guo et al., "A numerical model of cold-start stratification for proton exchange membrane fuel cells," *J. Tongji Univ. (Nat. Sci.)*, vol. 47, no. 1, pp. 104-112, 2019.

[2] J. Feng, Z. Zhan, X. He et al., "PEM study on water-heat balance during startup of fuel cell in low-temperature environment," *J. Wuhan Univ. Technol. (Transp. Sci. Eng.)*, vol. 41, no. 1, pp. 113-118, 2017.

[3] L. Yang, C. X. Cao, Q. Q. Gan et al., "Revealing failure modes and effect of catalyst layer properties for PEM fuel cell cold start using an agglomerate model," *Appl. Energy*, vol. 312, pp. 118792, 2022.

[4] P. He, Q. F. Xia, L. X. Jiang et al., "Effect of Pt loading on cathode catalytic layer during cold start," *J. Xi'an Jiaotong Univ.*, pp. 1-12, 2023.

[5] J. Zhao, W. H. Li, C. Q. Du et al., "Numerical simulation study of low temperature cold start of PEMFC under different operating and environmental conditions," *Acta Energiae Solaris Sin*., vol. 43, no. 6, pp. 460-466, 2022.

[6] L. Yao, J. Peng, J. B. Zhang et al., "Numerical simulation of cold start processes in proton exchange membrane fuel cell," *Chem. Ind. Eng. Prog*., vol. 38, no. 9, pp. 4029-4035, 2019.

[7] L. Wei, A. M. Dafalla, F. M. Jiang, "Effects of reactants/coolant non-uniform inflow on the cold start performance of PEMFC stack," *Int. J. Hydrogen Energy*, vol. 45, no. 24, pp. 13469-13482, 2020.

[8] Z. Liao, L. Wei, A. M. Dafalla et al., "Numerical study of subfreezing temperature cold start of proton exchange membrane fuel cells with zigzag-channeled flow field," *Int. J. Heat Mass Transf.*, vol. 165, p. 120733, 2021.

[9] L. Yang, C. X. Cao, Q. Q. Gan et al., "Revealing failure modes and effect of catalyst layer properties for PEM fuel cell cold start using an agglomerate model," *Appl. Energy*, vol. 312, p. 118792, 2022.

[10] J. Ko, W. Kim, T. Hong et al., "Impact of metallic bipolar plates on cold start behaviors of polymer electrolyte fuel cells (PEFCs)," *Solid State Ionics*, vol. 225, pp. 260-267, 2012.